CrossMark

J. Fluid Mech. (2015), *vol.* 775, *pp.* 1–23. © Cambridge University Press 2015
doi:10.1017/jfm.2015.287

Growth-and-collapse dynamics of small bubble clusters near a wall

A. Tiwari[1], C. Pantano[1] and J. B. Freund[1,2,†]

[1]Department of Mechanical Science and Engineering, University of Illinois at Urbana-Champaign, Urbana, IL 61801, USA

[2]Department of Aerospace Engineering, University of Illinois at Urbana-Champaign, Urbana, IL 61801, USA

(Received 25 July 2014; revised 3 May 2015; accepted 15 May 2015; first published online 16 June 2015)

The violent collapse of bubble clusters is thought to damage adjacent material in both engineering and biomedical applications. Yet the complexities of the root mechanisms have restricted theoretical descriptions to significantly simplified configurations. Reduced-physics models based upon either homogenization or arrays of idealized spherical bubbles do reproduce important gross cluster-scale features. However, these models neglect detailed local bubble–bubble interactions, which are expected to mediate damage mechanisms. To describe these bubble-scale interactions, we simulate the expansion and subsequent collapse of a hemispherical cluster of 50 bubbles adjacent to a plane rigid wall, explicitly representing both the asymmetric dynamics of each bubble within the cluster and the compressible-fluid mechanics of bubble–bubble interactions. Results show that the collapse propagates inward, as visualized in experiments, and that geometric focusing generates high impulsive pressures. This gross behaviour is nearly independent of the specific arrangement of bubbles within the cluster and matches predictions from the corresponding particle and homogenized models we consider. The peak pressure in the detailed simulations is associated with the centremost bubble, which causes a corresponding peak pressure on the nearby wall. However, the peak pressures in all cases are a small fraction – over a factor of ten times smaller in many cases – of those predicted in the corresponding reduced models. This is due to the enhanced focusing in the homogeneous model and the spherical constraint on each bubble in the particle models assessed. These would be important factors to consider in any subsequent predictions of wall damage based upon reduced models.

Key words: cavitation, biomedical flows, bubble dynamics

1. Introduction

Cavitation bubbles are important in many engineering and biomedical applications, playing a central role in erosion of hydraulic machines, underwater explosions, ultrasonic cleaning, and several types of non-invasive biomedical procedures. The destructive action of collapsing bubble clusters is widely recognized to have a role

† Email address for correspondence: jbfreund@illinois.edu

https://doi.org/10.1017/jfm.2015.287 Published online by Cambridge University Press

in erosion of turbomachinery components (Blake & Gibson 1987; Brennen 1995; Lauterborn & Kurz 2010). In recent years, the same basic mechanism has been harnessed for biomedical applications such as kidney-stone comminution and tissue fractionation (Zhong, Zhou & Zhu 2001; Bailey *et al.* 2003; Xu *et al.* 2004, 2008; Roberts *et al.* 2006; Freund, Colonius & Evan 2007; Coussios & Roy 2008; Freund, Shukla & Evan 2009). However, the detailed dynamics of these clusters are poorly quantified since the length scales ($\lesssim$100 μm) and time scales ($\lesssim$10 μs) during the final and most damaging stage of collapse challenge measurement technologies (Reisman, Wang & Brennen 1998; Konno *et al.* 2002; Krefting, Mettin & Lauterborn 2004; Matsumoto *et al.* 2005; Brujan *et al.* 2011). Optical diagnostics within the cloud are additionally difficult because of the large index of refraction mismatch at the bubble surfaces. Theoretical descriptions are likewise challenged by the multiple fluid phases and temporal and spatial scales that range from the microscopic scales of individual bubble dynamics to macroscopic average mixture dynamics of the bubbly liquid (van Wijngaarden 1968; Hansson & Mørch 1980; Caflisch *et al.* 1985; Omta 1987; d'Agostino & Brennen 1989; Commander & Prosperetti 1989; Kubota, Kato & Yamaguchi 1992; Zhang & Prosperetti 1994). Here, we simulate cluster dynamics with detailed accounting of the bubble length and time scales.

Spherically symmetric models (Rayleigh 1917; Plesset & Prosperetti 1977; Keller & Miksis 1980; Prosperetti & Lezzi 1986) provide a foundational understanding of single-bubble collapse: inertia associated with a rapid collapse increases internal pressures by orders of magnitude due to nearly adiabatic compression (Brennen 1995; Lauterborn & Kurz 2010). This same interchange of inertia and pressure is common in all such violent bubble dynamics, though asymmetry is well-understood to substantively change its details. If the collapse occurs adjacent to a wall, for example, the broken spherical symmetry can generate a re-entrant jet that is observed to be directed toward the wall (Kornfeld & Suvorov 1944). Both the high-speed jet itself and the shock waves it can emit as it penetrates through the bubble have been implicated as being responsible for the wall damage (Kornfeld & Suvorov 1944; Blake & Gibson 1987; Best 1993; Zhang, Duncan & Chahine 1993; Zhang *et al.* 2001; Johnsen & Colonius 2009).

For each bubble in a dense collapsing cluster, both walls and other bubbles are anticipated to likewise disrupt symmetry. The detailed collapse and damage mechanism of a collapsing cluster is thus less clear. High-speed movies of cloud collapse, the damage patterns on the adjacent material surfaces, and pressure measurements all suggest that the overall phenomenology is similar to a single bubble. Clusters appear to collapse inward, focusing energy in some central region where damage is greatest (Hansson & Mørch 1980). Visualizations and pressure measurements on hydrofoil surfaces also suggest the generation and inward focusing of shock waves during the cloud collapse (Reisman *et al.* 1998). Recent acoustic measurements and visualizations show that the peak pressures during collapse can even exceed that of a free-field single bubble of the same maximum radius, presumably due to the focusing of the collapsing cluster (Brujan, Ikeda & Matsumoto 2012), though these measurement lack sufficient resolution to identify specific mechanisms.

The geometric complexity of a collapsing bubble cluster, with each bubble potentially displaying its own complex asymmetric behaviour, has motivated the development of simplified homogeneous-mixture models that neglect the details of bubble-scale dynamics (van Wijngaarden 1968; Hansson & Mørch 1980; Caflisch *et al.* 1985; d'Agostino & Brennen 1989; Commander & Prosperetti 1989; Kubota *et al.*

https://doi.org/10.1017/jfm.2015.287 Published online by Cambridge University Press

1992; Zhang & Prosperetti 1994; Smereka 2002; Seo, Lele & Tryggvason 2010; Ando, Colonius & Brennen 2011; Fuster & Colonius 2011). These are generally based on a volume- or ensemble-averaging that is consistent with smaller variation of pressure over the bubble length scales. Analysis of such models suggests that the geometric collapse is accompanied by the generation and inward propagation of a bubbly shock wave that focuses to generate very high pressures at the cloud centre (Wang & Brennen 1999; Matsumoto & Yoshizawa 2005). These results suggest particularly violent collapse of bubbles near the focus. Our study examines this region in particular detail because of its importance and because it seems beyond the capabilities of current experimental diagnostics to quantify.

Experiments and simulations in idealized configurations show the types of interactions that can be anticipated in realistically disorganized bubble clusters. Bremond *et al.* (2006) set up a regular planar array of 37 bubbles and show that upon collapse there are large aspherical bubble deformations and re-entrant jetting toward the cluster centre. Boundary integral simulations of up to 16 bubbles by Chahine & Duraiswami (1992) show a similar inward propagation of collapse with large non-spherical bubble deformations and the onset of re-entrant jets. These simulations unfortunately were not continued through the collapse since the numerical scheme was incapable of representing topological changes of the bubbles. Any role of finite speed of sound in the liquid or non-uniform gas behaviour in the bubbles was neglected. To account for bubble–bubble interactions, small asymmetries in bubble shape have been modelled with multipole corrections to long-range interactions (Blake *et al.* 1999; Bui *et al.* 2006) within small ($\leqslant$25 bubble) clusters, but these are unable to represent details of highly deformed bubbles.

Despite these advances, the detailed bubble-scale dynamics of a cluster collapse remain poorly quantified, though we can anticipate that they are important for material damage, especially at the cluster centre. Quantifying these dynamics motivates our detailed three-dimensional bubble cluster simulations. We solve the compressible-fluid multiphase-flow equations, which include all mesh-resolved bubble–bubble interactions and the non-spherical dynamics of each bubble within the cluster. As a model system, we particularly focus on collapsing hemispherical 50-bubble clusters adjacent to a rigid wall. Our clusters are generated randomly, but given the anticipated importance of bubble–bubble interactions, we expect that the specific details of any particular collapse will be somewhat sensitive to the initial bubble arrangement. We therefore consider multiple statistically equivalent random distributions. Anticipating that the bubbles near the centre are most important, we also consider a special arrangement in which a central bubble is positioned on a symmetry axis near the cluster centre. The expansion of the cluster is driven by the initial over-pressure in the bubbles, which is also varied between cases. This dependence is particularly important for biomedical applications, where cavitation-based therapeutic actions have been enhanced by optimizing repetition rates and intensities of ultrasound pulses or shock waves (Sapozhnikov *et al.* 2002; Xu *et al.* 2005*a*,*b*; Pishchalnikov *et al.* 2006; Xu, Fowlkes & Cain 2006).

The specific simulation configuration and the numerical method are explained § 2. The detailed simulation results are discussed in § 3 and compared with reduced models in § 4. The key findings are summarized in § 5.

2. Simulation details

2.1. *Initial configurations*

The 50 initially spherical bubbles, each of radius $R_0 = 0.3$ mm, are positioned randomly next to the wall at $x = 0$, each fully within a hemisphere of radius

https://doi.org/10.1017/jfm.2015.287 Published online by Cambridge University Press

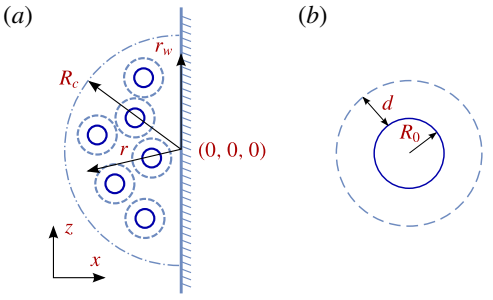


FIGURE 1. (Colour online) Schematic of (*a*) a random but non-overlapping arrangement of bubbles of radius R_0 within the hemisphere of radius R_c, and (*b*) a representative bubble with the exclusion constraint d.

$R_c = 7.37$ mm centred at (0, 0, 0) and subject to the constraint that the initial separation between the surfaces of any two bubbles is greater than $2d = 1.4$ mm (figure 1). The minimum distance between a bubble surface and the wall is also d, so we do not consider cases in which the bubbles sit directly on the wall, though this might be an important factor in damage in some cases. Polydispersity can also be an important factor (Wang 1999; Shimada, Matsumoto & Kobayashi 2000; Ando *et al.* 2011), which we do not consider in these idealized models.

The bubble sizes in our simulations are similar to those seen in similar experimental studies, such as those of Kameda & Matsumoto (1996) and Kameda *et al.* (1998), and the initial inter-bubble spacings are selected to give a relatively low initial gas volume fraction (6.5×10^{-3}), such as is also observed (Kameda & Matsumoto 1996; Kameda *et al.* 1998; Bremond *et al.* 2006; Arora, Ohl & Lohse 2007). However, the number of bubbles represented is considerably smaller owing to computational cost. The 50 bubbles simulated reflect a compromise between accounting for detailed bubble–bubble interactions of the kind expected in an actual cloud and keeping the computational cost manageable with available computational resources.

To generate this configuration, bubbles were sequentially added at random positions in this hemisphere subject to the separation constraint. The entire simulation domain in Cartesian coordinate spanned $(x, y, z) \in [-30, 0] \times [-30, 30] \times [-30, 30]$ mm^3. One-dimensional characteristic boundary conditions are used to model an infinite fluid-filled domain beyond the simulation domain.

All initial velocities are zero though motion starts immediately due to the initial pressure $p_g > p_\infty$ in the bubbles, where $p_\infty = 0.1$ MPa is the ambient pressure. The initial pressure is uniform within each bubble and decays smoothly into the liquid with a hyperbolic tangent profile $\tanh[(r_i - R_0)/(R_0 + d)]$, where r_i is the distance of a point in the domain from the centre of the nearest bubble i. We use this mollified pressure field to prevent sharp pressure jumps at the bubble surfaces and the resulting emission of spurious compression waves. It decays within the initial bubble separation distance $2(R_0 + d)$ and thus provides a better characterized initial condition than, say, a $1/r$ pressure decay by removing bubble–bubble pressure interaction from the initial condition. We shall see that the pressure due to the bubble dynamics quickly overwhelms this initial smooth distribution. The liquid is water with initial density $\rho_{l,0} = 1000$ kg m^{-3}. The initial gas density $\rho_{g,0}$ is obtained from the barotropic relation $p_g/p_\infty = (\rho_{g,0}/\rho_\infty)^{\gamma_g}$, with $\rho_\infty = 1$ kg m^{-3}, and $\gamma_g = 1.4$.

Initial bubble over-pressure ratios are $p_g/p_\infty = 2.5$, 5, and 7.5, and we consider four different random arrangements (A, B, C, and D) as summarized in table 1. These

https://doi.org/10.1017/jfm.2015.287 Published online by Cambridge University Press

Case	Arrangement	r_{cm} (mm)	p_g (MPa)	Number of bubbles
A1	A	1.645	0.25	50
A2	A	1.645	0.5	50
A3	A	1.645	0.75	50
B2	B	1.222	0.5	50
C2	C	2.272	0.5	50
D2	D	1.000	0.5	50
D2′	D′	2.498	0.5	49
D2*	D*	1.000	0.5	1
D3*	D*	1.000	0.75	1

TABLE 1. Cases simulated, with r_{cm} the initial radial location of the centremost bubble and p_g the initial bubble pressure.

initial over-pressures are sufficiently strong to cause violent collapses, but more intense pressures are expected in some applications (Brujan *et al.* 2011, 2012). We limit our simulations to these pressures to facilitate numerical convergence for our observables. The specific bubble locations are tabulated in supplementary data available at http://dx.doi.org/10.1017/jfm.2015.287, tables S1 and S2. Case D2 is a variant of arrangement D, in which the centremost bubble is placed at $x = R_0 + d = 1$ mm and $y = z = 0$. Throughout the paper, we refer to the centremost bubble as the bubble closest to the coordinate system origin, near the wall, not the bubble closest to the geometrical centre of the cluster. Similarly, arrangement D′ is derived from D by removing this centremost bubble, and arrangement D* is a single-bubble case with only the centremost bubble of D.

The liquid is water, which is modelled with a stiffened equation of state (Menikoff & Plohr 1989), and the gas inside the bubbles is air modelled as ideal; the equation of state parameters are those of Saurel & Abgrall (1999*b*). Based on R_0, the characteristic speed $\sqrt{p_g/\rho_{l,0}}$, and water-like kinematic viscosity $\nu = 10^{-6}$ m^2 s^{-1}, the Reynolds numbers range from $Re = 4743$ to 8216, which justifies neglecting viscosity in the simulations. The corresponding Weber numbers for an air–water surface tension 0.07 N m^{-1} range from 1071 to 3214, which similarly justifies neglect of surface tension. Though in some cases surface tension and viscosity can influence some details of jetting and fragmentation during the final stages of a bubble collapse (Popinet & Zaleski 1999, 2002), we neglect those effects to focus on bubble–bubble interactions in this study. Similarly, thermal and mass diffusion are neglected, as is phase change, though it has been considered in some other studies (Esmaeeli & Tryggvason 2004*a*,*b*; Hardt & Wondra 2008; Lauer *et al.* 2012). For the current conditions, the liquid pressure remains above the saturation pressure at room temperature.

2.2. *Numerical methods*

Full details of the numerical scheme along with detailed convergence studies and comparisons with semi-analytic solutions are reported in our previous paper (Tiwari, Freund & Pantano 2013), and are thus only summarized here. The gas–liquid description is based upon a variant of the Baer–Nunziato model (Baer & Nunziato 1986) by Saurel & Abgrall (1999*a*), which uses a mixture description to represent the phases without any explicit Lagrangian tracking of the interface. The interfaces are thus thin mixture regions represented on a fixed mesh. These interfaces are

https://doi.org/10.1017/jfm.2015.287 Published online by Cambridge University Press

maintained thin via thermodynamically consistent localized 'sharpening' terms added to the governing equations (Tiwari *et al.* 2013):

$$\mathscr{R}_g = \mathscr{U}_0 \boldsymbol{n} \cdot (\boldsymbol{\nabla}(\epsilon \boldsymbol{n} \cdot \boldsymbol{\nabla}(\rho_g \alpha_g)) - (\alpha_l - \alpha_g)\boldsymbol{\nabla}(\rho_g \alpha_g)), \tag{2.1}$$

where the gradient of gas mass fraction, $\boldsymbol{\nabla}(\rho_g \alpha_g)$, localizes its action to the interface in the corresponding transport equation

$$\frac{\partial \rho_g \alpha_g}{\partial t} + \boldsymbol{\nabla} \cdot (\rho_g \alpha_g \boldsymbol{u}) = \mathscr{R}_g. \tag{2.2}$$

In (2.1), $\mathscr{U}_0$ is a sharpening strength, $\boldsymbol{n}$ is the interface normal, and $\epsilon \approx 1.5\Delta x_{min}$, where Δx_{min} is the refined mesh spacing (discussed subsequently). This ϵ factor thus restricts the thickness of the interface. The remaining parameters are the gas density ρ_g, the mixture velocity $\boldsymbol{u}$, the gas volume fraction α_g, and the liquid volume fraction α_l. The corresponding $\mathscr{R}$-like terms in the other transport equations are designed to be thermodynamically consistent with the same mixture law, in order for the thermodynamic state to remain collectively consistent within the thin mixture region (Tiwari *et al.* 2013). This avoids the spurious oscillations that can occur for sharp interfaces when thermodynamic consistency is not respected within the thin interface zone. It also allows interfaces to be always sufficiently resolved by the underlying mesh.

The compressible-flow equations that represent both fluids are discretized on a fixed Cartesian mesh, and are solved using a finite-volume description based upon the common reconstruct-evolve-average approach (Toro 2006). A total variation diminishing third-order Runge–Kutta method (Gottlieb & Shu 1988) is used for time integration. The necessary Riemann problems are solved approximately using the HLLC method (Johnsen & Colonius 2006; Toro 2006). A fifth-order WENO scheme (Jiang & Shu 1996; Titarev & Toro 2004) is employed for spatial reconstruction.

The algorithm is implemented in an adaptive mesh refinement (AMR) (Deiterding *et al.* 2006) framework per the specifications discussed in the following subsection. A typical simulation used four levels of adaptive refinement, which corresponds to about 2×10^7 computational cells for the initial configurations. This same local resolution would require about 2×10^9 uniformly distributed mesh points for the domain studied. The total cost of a typical simulation presented here is 144 h on 120 cores with the Intel HP X5650 2.66 GHz 6C processor.

2.3. *Resolution assessment*

The numerical algorithm has been validated extensively against many test problems, including single-bubble collapses, in our previous paper (Tiwari *et al.* 2013). There, we reported excellent agreement between our detailed three-dimensional single-bubble simulations and highly accurate spherically symmetric Keller–Miksis solutions. Here we only confirm resolution sufficiency for the present configurations. The simulations discussed in § 3 used a minimum AMR mesh spacing $\Delta x_{min} = 39$ μm, which corresponds to $n = R_0/\Delta x_{min} = 7.7$ cells per initial bubble radius. We first performed a detailed resolution study on the single-bubble case D3* (table 1). Figure 2 shows the convergence of gas volume and total kinetic energy history with grid refinement. The effect of resolution on actual cluster simulation is discussed further in the next section.

https://doi.org/10.1017/jfm.2015.287 Published online by Cambridge University Press

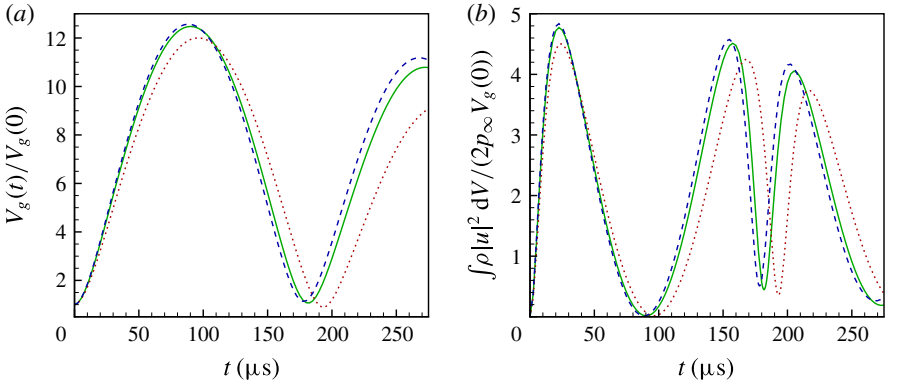


FIGURE 2. (Colour online) (*a*) Gas volume history, and (*b*) total kinetic energy for case D3* at different resolutions n: ·····, $n = 3.8$; ——, $n = 7.7$; – – –, $n = 15.4$.

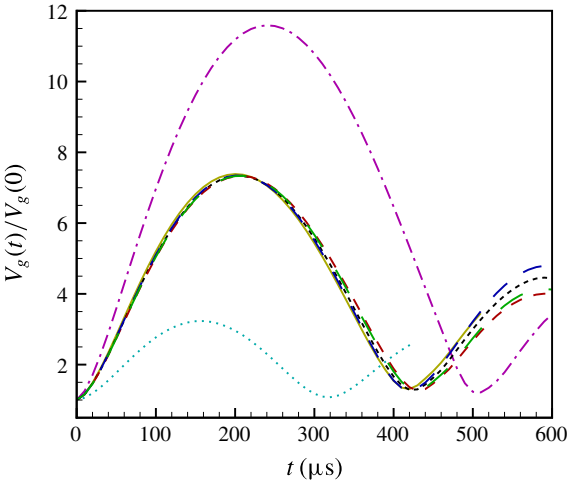


FIGURE 3. (Colour online) Gas volume history: ·····, A1; - - - -, A2; – – –, B2; ———, C2; ——, D2; — · —, A3 listed in table 1; and ——, D2 at double resolution ($n = 15.6$).

3. Simulation results

3.1. *Overall cluster dynamics*

The cluster gas volume histories $V_g(t)$ for the 50-bubble cases are shown in figure 3, including a confirmation of mesh independence for case D2. The effect of initial pressure is obvious. Higher initial pressures (case A3) lead to larger expansion of the bubbles and longer times to collapse; lower initial pressures (case A1) do the opposite.

For fixed initial pressure but different random bubble distributions, the gas volume history for all four $p_g/p_\infty = 5$ cases (A2, B2, C2, and D2) are similar. This suggests that our cluster is sufficiently large that the particular dynamics of the random arrangements approximately average out and do not affect much this global quantity. A well-crafted homogenization might therefore be evaluated for reproducing this behaviour. However, despite the similarities of the overall collapse, there is a

https://doi.org/10.1017/jfm.2015.287 Published online by Cambridge University Press

Case	p_{peak} (MPa)	p_{peak}/p_g	t_{max} (μs)
A1	0.26	1.04	290
A2	1.49	2.98	395
B2	2.87	5.74	402
C2	0.96	1.92	390
D2	2.64	5.28	400
D2′	0.80	1.60	390
A3	4.98	6.64	477

TABLE 2. p_{peak} and t_{max} for different initial arrangements.

factor-of-three case-to-case difference in the peak pressures within the cluster (table 2). (Doubling the resolution to $n = 15.6$ for case D2 leads to a pointwise variation of less than 7 % in peak pressure, which is far less than the arrangement-to-arrangement variability.) We also note that for all the cases considered, the peak pressures exceed the initial overpressure ($p_{peak}/p_g > 1$). For the expansion and collapse of an isolated single bubble in a free field, the Keller–Miksis model (Keller & Miksis 1980) gives $p_{peak} = 0.24$, 0.46, and 0.67 MPa for $p_g = 0.25$, 0.5, and 0.75 MPa, respectively, implying $p_{peak}/p_g < 1$. Thus, we can already conclude that bubble–bubble interactions promote some form of pressure amplification. The specific interactions leading to this are discussed in the following subsection.

3.2. *Detailed bubble dynamics*

Figure 4 shows the entire expansion and collapse of the D2 cluster. The initial mollified pressure and the corresponding zero-velocity initial condition at $t = 0$ μs are seen in figures 4(*a*) and 4(*i*). By $t = 20$ μs, all the bubbles are obviously expanding, with a nearly uniform high pressure spanning the cluster (4*b*). However, the kinetic energy (4*j*) shows that the bubbles toward the centre of the cluster are expanding relatively slowly or not at all. This delay is due to the collective focusing of a compression wave generated by each over-pressured bubble of the initial condition. The outermost bubbles, which at this time are exposed to the lower ambient pressure, are the least confined by this compression. This trend reverses by $t = 170$ μs, when a relatively low pressure now spans the core (4*c*) and drives a delayed expansion of the inner bubbles (4*k*). As was seen in figure 3, by $t = 200$ μs the cluster is near its maximum overall volume, though not all bubbles are in phase with this overall behaviour. At this time, the inner bubbles are still expanding in a low-pressure region (4*d*) while the outer bubbles have begun to collapse, as seen by their kinetic energy and deforming shapes (4*l*).

We note that despite the nearly spherical bubble shape in the expansion phase up to $t = 200$ μs in figure 4(*d*), the non-uniform pressure field sets the directionality and potentially initiates the jetting during the collapse phase. At this time, we also see bubble shapes consistent with the onset of jetting behaviour. These and subsequent frames in the visualized time series show that the collapse starts in the outer regions.

The evolution of the pressure around $t = 200$ μs is further quantified in figure 5, which shows minimum pressure p_{min} versus the radial distance r. We see that p_{min} is decreasing from $t = 200$ to 240 μs near the central region while increasing in the outer region, which confirms that the central bubbles are still expanding while the outer bubbles have begun to collapse.

https://doi.org/10.1017/jfm.2015.287 Published online by Cambridge University Press

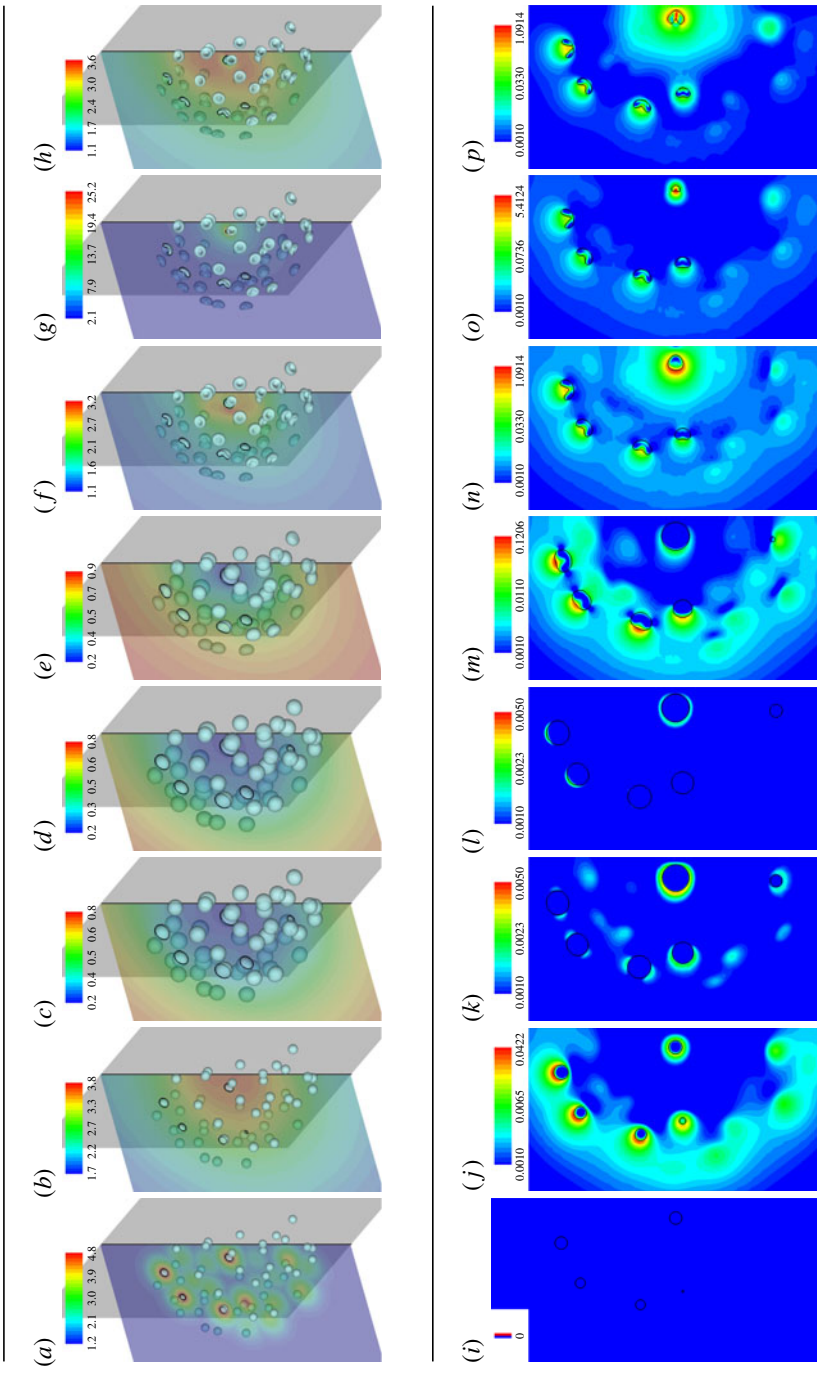


FIGURE 4. (Colour online) (*a–h*) Bubble shapes and pressure contours and (*i–p*) kinetic energy contours for case D2 in table 1. Note logarithmic scale for kinetic energy contours. (*a,i*) $t = 0$ μs, (*b,j*) $t = 20$ μs, (*c,k*) $t = 170$ μs, (*d,l*) $t = 200$ μs, (*e,m*) $t = 320$ μs, (*f,n*) $t = 390$ μs, (*g,o*) $t = 400$ μs, (*h,p*) $t = 410$ μs.

https://doi.org/10.1017/jfm.2015.287 Published online by Cambridge University Press

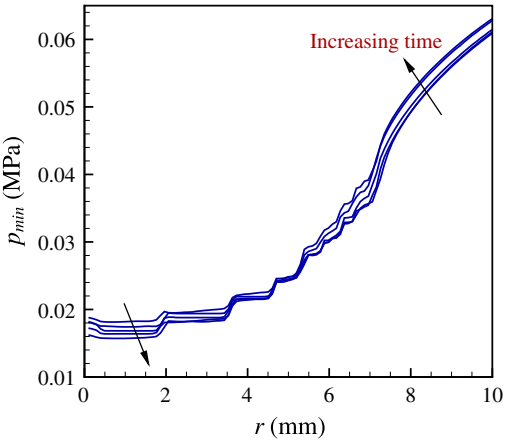


FIGURE 5. (Colour online) The pressure minima $p_{min}(r)$ for case D2 versus the radial distance r from the cluster centre (shown in figure 1*a*) for times $t = 200$–240 μs, showing the transition from expansion to collapse. Equal time intervals are shown with increasing t.

By $t = 320$ μs, kinetic energy suggests a strong jetting toward the cluster centre (figure 4*m*), which is confirmed by the corresponding visualizations of velocity (not shown). However, at this same time the centremost bubble retains a much larger volume, and is still in a relatively low-pressure region (4*e*). This is reversed by $t = 390$ μs (figure 4*f*,*n*), when the collapse has reached the centremost bubble with an apparent focusing of kinetic energy and pressure associated with the inward progress of collapse. The highest kinetic energy is now tightly focused on the side of the centremost bubble that is furthest from the wall. Just 10 μs later at $t = 400$ μs, this bubble is almost fully collapsed (4*g* and 4*o*), which is followed by a fast re-expansion by $t = 410$ μs (4*h* and 4*p*). We note from figure 3 that the onset of re-expansion occurs when the overall gas volume is still decreasing. Liquid inertia generates very high pressure in the centremost bubble in a short time, which drives its rapid re-expansion. Peak pressure in the domain is generated during the fast collapse and re-expansion of the centremost bubble just before the overall cluster attains minimum bubble volume. Table 2 and figure 3 show a similar trend for all the cases considered.

The pressure field at the time of overall peak pressure is quantified in figure 6, where we plot the maximum pressure p_{max} versus the radial distance r and on the wall for cases A2 to D2, which have the same initial over-pressure in the bubbles (table 1). For all cases, the peak pressure is associated with the centremost bubble, the location of which is also shown schematically in the figure. This is the case in the bulk fluid and for the wall pressures. Visualization of the wall pressures in figure 7 show that it is relatively simple and axisymmetric despite the complexity of the bubble dynamics. The same is true for case D2′, which is equivalent to case D2 though with the centremost bubble removed. The peak pressure is now obviously associated with the next-to-centremost bubble at $r_{cm} = 2.50$ mm for D2, now filling the role of the centremost bubble for D2′.

The collapse of the centremost bubble for cases A2 to D2 is visualized in detail in figure 8, which shows momentum vectors $\rho\boldsymbol{u}$ at $t = 400$ μs projected onto the plane that intersects both the centre of the centremost bubble and the axis of symmetry of the hemisphere that defines the bubble cluster (see figure 1*a*). Here we see

https://doi.org/10.1017/jfm.2015.287 Published online by Cambridge University Press

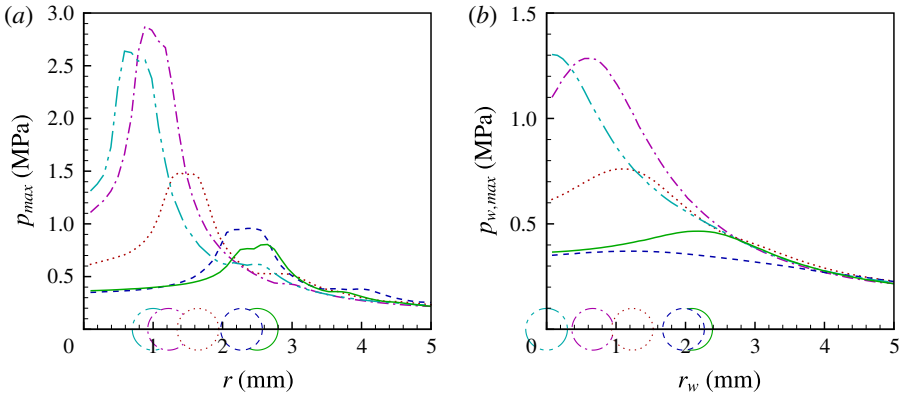


FIGURE 6. (Colour online) The pressure maxima at the time when peak pressure is observed for cases · · · · · ·, A2; — · —, B2; – – –, C2; — · · —, D2; ——, D2′: (*a*) versus the radial distance r from the cluster centre, and (*b*) along the wall at radius r_w from the centre of the cluster. Circles indicate the radial location of the centremost bubble.

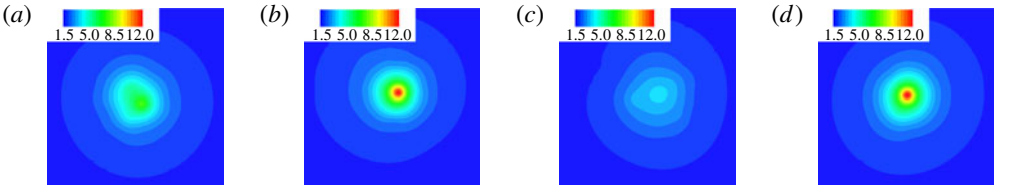


FIGURE 7. (Colour online) Wall pressure at the instant of peak wall pressures. Note the logarithmic colour scale, with units of pressure $\times 10^5$ Pa. (*a*) A2, (*b*) B2, (*c*) C2, (*d*) D2.

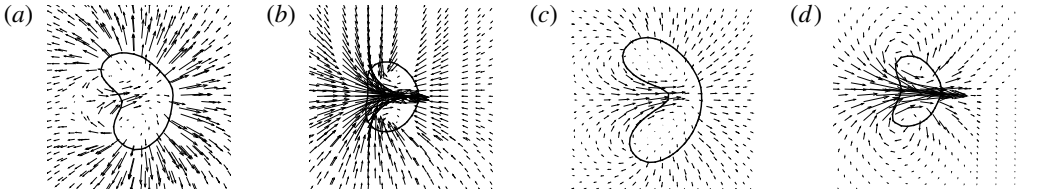


FIGURE 8. Momentum vectors along the plane normal to the x–y plane containing the centre of the hemisphere and the centre of the centremost bubble at $t = 400$ μs for: (*a*) A2, (*b*) B2, (*c*) C2, (*d*) D2.

the asymmetrical bubble dynamics, particularly the re-entrant jetting. The specific environment in the cluster of the centremost bubble determines the details of this jetting and thereby the actual peak pressures and potential for wall damage. It is clear in figure 8 that these bubbles collapse differently in different cases. This variation would be anticipated to give rise to significant collapse-to-collapse variability in damage to adjacent material, though thorough investigation of that is beyond the scope of this study.

To quantify the kinetic energy associated with the non-spherical deformations, we consider the centremost and, for contrast, outermost bubbles of case A2. The gas volume histories $V_{g,i}(t)$ for these two bubbles are shown in figure 9(*a*). We note that

https://doi.org/10.1017/jfm.2015.287 Published online by Cambridge University Press

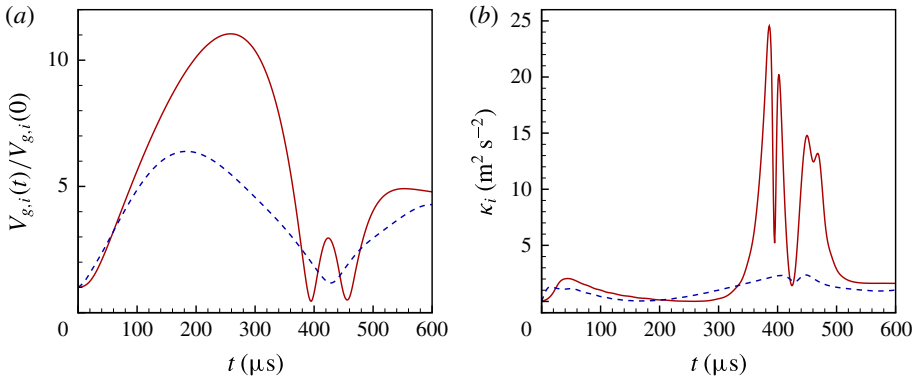


FIGURE 9. (Colour online) (*a*) Gas volume histories and (*b*) mass specific kinetic energy of the liquid surrounding the bubbles: ——, centremost; – – –, outermost.

the volume of the centremost bubble has a maximum near 270 μs and local minima near 400 and 460 μs, while the outermost bubble has a maximum near 180 μs and a minimum near 430 μs. We now define a region surrounding a bubble in which we compute the mass-specific non-translational average kinetic energy $\kappa_i(t)$ of the liquid. This region is a sphere concentric with the bubble's centre of mass, and its radius is such that it encloses a fixed liquid mass m_0:

$$\iiint \rho(\boldsymbol{x}, t)\,\mathrm{d}\boldsymbol{x} = m_0. \tag{3.1}$$

We use the initial liquid density $\rho_{l,0}$ and initial bubble radius R_0 to define this fixed mass:

$$m_0 = \tfrac{4}{3}\pi\,\rho_{l,0}[(2R_0)^3 - R_0^3]. \tag{3.2}$$

The average kinetic energy $\kappa_i(t)$ is then

$$\kappa_i(t) = \frac{1}{2m_0}\iiint \rho(\boldsymbol{x}, t)|\boldsymbol{u}(\boldsymbol{x}, t) - \bar{\boldsymbol{u}}(\boldsymbol{x}, t)|^2\,\mathrm{d}\boldsymbol{x}, \tag{3.3}$$

where $\boldsymbol{u}$ is the velocity and $\bar{\boldsymbol{u}}$ is the average velocity in the spherical region,

$$\bar{\boldsymbol{u}}(t) = \frac{1}{m_0}\iiint \rho(\boldsymbol{x}, t)\boldsymbol{u}(\boldsymbol{x}, t)\,\mathrm{d}\boldsymbol{x}, \tag{3.4}$$

which we subtract from the velocity in (3.3) to remove the translational component of velocity.

The kinetic energy histories for the two bubbles are shown in figure 9(*b*). We observe that the kinetic energies increase initially due to the initial acceleration of the bubbles. They reach local maximum, then reduce, and nearly vanish near maximum gas volume. This is consistent with the spherical bubble shapes observed in figure 4 during the expansion phase: if the bubbles remain spherical then kinetic energy must vanish when the gas volume attains local maximum or minimum. After this, the kinetic energies again increase during the collapse phase, and we note that kinetic energies do not vanish at the subsequent local minima or maxima. This is again consistent with the non-spherical bubble shapes and the kinetic energy contours

https://doi.org/10.1017/jfm.2015.287 Published online by Cambridge University Press

observed in figure 4 during the collapse phase, and the momentum vectors observed in figure 8. This is clearly indicative of the loss in energy to the liquid jets, which leads to the weaker rebound of the bubbles observed in figure 9(*a*).

Based on the gas volume history in figure 3, we note that though the central bubbles undergo relatively stronger collapses, the over-pressures in our simulations are such that the average strength of bubble collapse is relatively weak (Philipp & Lauterborn 1998; Lindau & Lauterborn 2003). In this weak-strength but strong-interaction regime, the energy lost to re-entrant jetting is higher than viscous, thermal, and acoustic damping mechanisms. This was anticipated by Brennen (2002), who suggested that more kinetic energy might be lost in bubble fragmentation than all other damping mechanisms. Similarly, Delale & Tunc (2004) developed a modified Rayleigh–Plesset model to account for fission losses during rebound. The other mechanisms are expected to become relatively more important in more intense collapses (Fuster, Dopazo & Hauke 2011), particularly for vapour-filled cavities (Akhatov *et al.* 2001). In strong collapses of relatively weakly interacting bubbles, they would behave more as individual units, and the energy loss to kinetic energy via jetting or similar mechanisms could be much smaller compared to the dominant damping for spherical collapses. Quantifying in detail any switch-over of the dominant damping mechanisms would require more challenging simulations of more violent bubble collapses.

We now consider the dependence upon initial overpressure, examining cases A1 to A3 from table 1 with pressure ratios $p_g/p_\infty = 2.5$, 5.0, and 7.5. The gas volume histories in figure 3 suggest that the high pressure will lead to both larger volumes of individual bubbles and bubble surfaces that more closely interact. Therefore, we anticipate both more violent dynamics associated with individual bubbles and stronger bubble–bubble interactions. The peak pressures generated during the final stage of the collapse bear this out (table 2). For comparison, we list the ratio of the peak pressure generated to the initial over-pressure in the bubbles p_{peak}/p_g. Almost no pressure amplification is observed for the case A1 ($p_g/p_\infty = 2.5$), which suggests that the bubbles in this case behave approximately independently. Indeed, corresponding visualizations suggest that the bubbles remain roughly spherical (figure 11). However, interactions become pronounced with increasing initial over-pressure for cases A2 and A3, suggesting that collective bubble behaviour dominates at these large initial over-pressures. The peak pressure at radius r shown in figure 10 is nearly flat for case A1 ($p_g/p_\infty = 2.5$) but increases significantly for A3 ($p_g/p_\infty = 7.5$) and is obviously associated with the radial location of the centremost bubble.

4. Comparison with simplified models

The most common homogenization procedure for bubbly flows is based upon the scale separation between long-range pressure interactions across the bubbly liquid and the dynamics of the small bubbles (van Wijngaarden 1968, 1972; Caflisch *et al.* 1985; Commander & Prosperetti 1989; Zhang & Prosperetti 1994; Brennen 1995). On one hand, the clusters we consider in this study are too small to guarantee that results could be reproduced with such a model. We observed, for example, in § 3 that the inward pressure focusing during the cluster collapse appears to be of the same scale as the bubbles, particularly near the pressure focus. On the other hand, the insensitivity to bubble details of the overall cluster dynamics, such as the gas volume fraction in figure 3, suggests that comparisons will be informative. For the homogeneous-mixture model we consider in the following subsection, we show that a homogenized description produces reasonable results despite the absence of

https://doi.org/10.1017/jfm.2015.287 Published online by Cambridge University Press

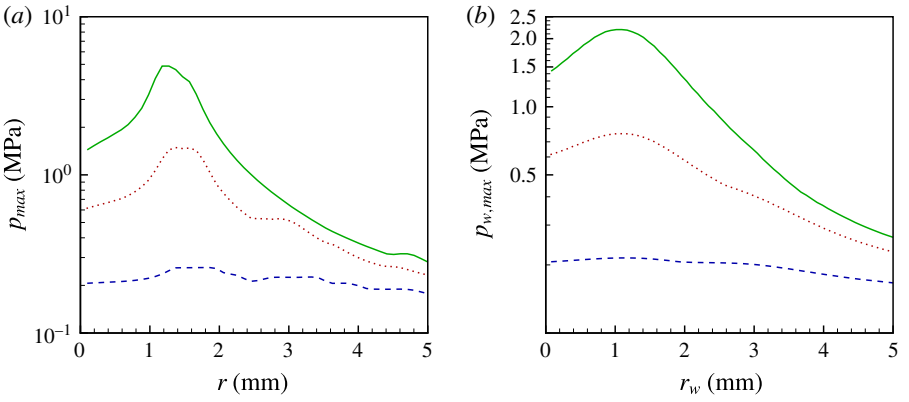


FIGURE 10. (Colour online) The pressure maxima $p_{max}(r,\ t)$ at the time when peak pressure is observed for cases – – –, A1; · · · · · ·, A2; ——, A3: (*a*) versus the radial distance r from the cluster centre and (*b*) along the wall at radius r_w from the centre of the cluster.

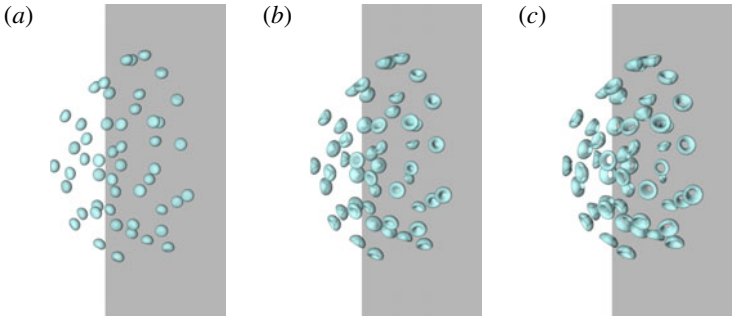


FIGURE 11. (Colour online) Bubble shapes near the minimum volume for cases (*a*) A1, $t = 300$ μs; (*b*) A2, $t = 400$ μs; (*c*) A3, $t = 480$ μs.

a large scale separation. Although this is encouraging, we are unable to provide any conclusion regarding the performance of these models in cases with a greater scale separation between cluster- and bubble-scale dynamics. The principal goal of our bubble-detailed simulations is to represent the dynamics near the centre of the cluster, where the homogeneous-mixture assumptions fail even in huge clusters for which a large scale separation is easier to achieve. A model that does not rely upon the long-wavelength approximation seems essential, so we more closely evaluate particle-like descriptions of each bubble. In this case, bubble–bubble interactions are explicitly included but the dynamics of each bubble is simplified. We consider such a representation in § 4.2.

4.1. *Homogeneous-mixture model*

The homogeneous-mixture barotropic model we consider, like many such models that have been employed, is based on two main assumptions (van Wijngaarden 1972; Brennen 1995): (i) both the bubble sizes and the inter-bubble spacings are small relative to the pressure variation scale (wavelength) in the surrounding flow field, and

https://doi.org/10.1017/jfm.2015.287 Published online by Cambridge University Press

(ii) the natural frequencies of the bubbles are large relative to the time scales of the overall flow field. The resulting mixture mass and momentum equations are similar to those for single-phase flows (van Wijngaarden 1972; Brennen 1995):

$$\frac{\partial \rho}{\partial t} + \boldsymbol{\nabla} \cdot (\rho \boldsymbol{u}) = 0, \tag{4.1a}$$

$$\frac{\partial \rho \boldsymbol{u}}{\partial t} + \boldsymbol{\nabla} \cdot (\rho \boldsymbol{u} \otimes \boldsymbol{u}) + \boldsymbol{\nabla} p = 0, \tag{4.1b}$$

where ρ is the mixture density, p is the mixture pressure and $\boldsymbol{u}$ is the mixture velocity. A suitable barotropic relation completes the system. For isentropic flows without mass transfer, this is (Brennen 1995)

$$\frac{1}{\rho}\left(\frac{\partial \rho}{\partial p}\right)_s = \frac{\alpha_1}{\rho_1}\left(\frac{\partial \rho_1}{\partial p}\right)_{s_1} + \frac{\alpha_2}{\rho_2}\left(\frac{\partial \rho_2}{\partial p}\right)_{s_2}, \tag{4.2}$$

where $\alpha_{1,2}$, $s_{1,2}$ and $\rho_{1,2}$ are respectively the volume fractions, entropies, and densities of the respective phases, and s is the mixture entropy. The stiffened equation of state we use (Menikoff & Plohr 1989) gives

$$\frac{1}{\rho_k}\left(\frac{\partial \rho_k}{\partial p}\right)_{s_k} = \frac{1}{\gamma_k (p + p_k^\infty)}, \tag{4.3}$$

and thus

$$\frac{p + p_k^\infty}{\rho_k^{\gamma_k}} = \text{constant}, \tag{4.4}$$

where p_k^∞ and γ_k are the stiffened gas equation of state parameters of phase $k = 1, 2$. This state equation models the physics of the molecular attraction in the liquid as if it were an ideal gas pre-compressed with pressure p^∞, which thus serves as a model parameter. Following Saurel & Abgrall (1999*b*), we take $p_1^\infty = 600$ MPa to model liquid water, for which the polytropic exponent $\gamma_1 = 4.4$ produces the correct speed of sound. For the gas phase, we take $p_2^\infty = 0$ and $\gamma_2 = 1.4$. Together (4.2) and (4.3) provide a mixture pressure–density relation,

$$\frac{\mathrm{d}\rho}{\mathrm{d}p} = \rho \left[\frac{\alpha_1}{\gamma_1 (p + p_1^\infty)} + \frac{\alpha_2}{\gamma_2 (p + p_2^\infty)}\right], \tag{4.5}$$

from which $p(\rho)$ closes (4.1).

To facilitate comparison, we specify an initial condition to match that of the detailed simulation. In doing this, most quantities are straightforward to select. The initial gas volume fraction α_0 and initial density ρ_0 of the homogeneous mixture are obtained by averaging, and the initial momentum is zero in both configurations. However, specifying the initial pressure (or, equivalently, mixture energy) is not straightforward. Setting a uniform pressure by averaging that of the detailed configuration does not conserve energy between the two configurations. Likewise, forcing conservation of total initial internal energy unphysically redistributes it between the liquid and gas in a way that disrupts the momentum balance between the two configurations (Brennen 1995).

To avoid ambiguity in the initial condition, we run new bubble-detailed simulations with an equivalent initial condition to facilitate correspondence. The bubbles and liquid

https://doi.org/10.1017/jfm.2015.287 Published online by Cambridge University Press

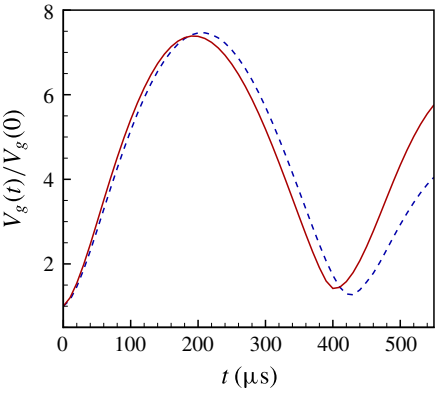


FIGURE 12. (Colour online) Gas volume history using: ——, the homogeneous-mixture model; – – –, the detailed simulation.

in the cluster hemisphere are given a uniform over-pressure p_g. Beyond the cluster, the pressure decays smoothly to p_∞ with the same hyperbolic tangent profile used in § 2. The arrangement matches the A configuration from table 1 and the parameters match that of case A2. The same uniform pressure is unambiguously used in the homogeneous-mixture model.

The same numerical solver is used for the homogeneous mixture, though without the interface correction terms (Tiwari *et al.* 2013), so the region fills the entire hemisphere. The other simulation conditions for the homogeneous-fluid configuration match those for the detailed configuration.

Figure 12 shows that the homogeneous-mixture model provides a qualitatively correct and reasonably accurate prediction of the overall gas volume history compared to the bubble-detailed simulation, especially up to the minimum-volume collapse point. After this point, it starts to deviate further, since the complexity of the actual bubble dynamics in the collapse cannot be reproduced by the model.

The radial pressure profiles for the detailed simulation during the final stage of the collapse are shown in figure 13(*a*,*b*). They are similar to the cases discussed in § 3, with peak pressure generation near the centremost bubble. In contrast, the corresponding profiles for the homogeneous-fluid model shown in figure 13(*c*,*d*) show that its collapse includes a strong compression wave that focuses to form a very high peak impulsive pressure (>23 MPa). The inward propagation and reflection from the wall of these waves is shown in figure 13(*c*). The re-expansion is also qualitatively different.

We thus conclude this section by noting that the pressure distributions obtained from the simplified model are fundamentally different throughout the simulation, which makes the volume history predicted by this same model seem surprisingly good.

4.2. *Bubble–particle models*

Particle-based models assume simple bubble dynamics but do not assume that cluster-scale pressure interactions are smooth (Parlitz *et al.* 1999; Doinikov 2004; Yasui *et al.* 2008; Lauterborn & Kurz 2010; Zeravcic, Lohse & Van Saarloos 2011). In the basic approach, the N bubbles comprising the cloud are assumed spherical

https://doi.org/10.1017/jfm.2015.287 Published online by Cambridge University Press

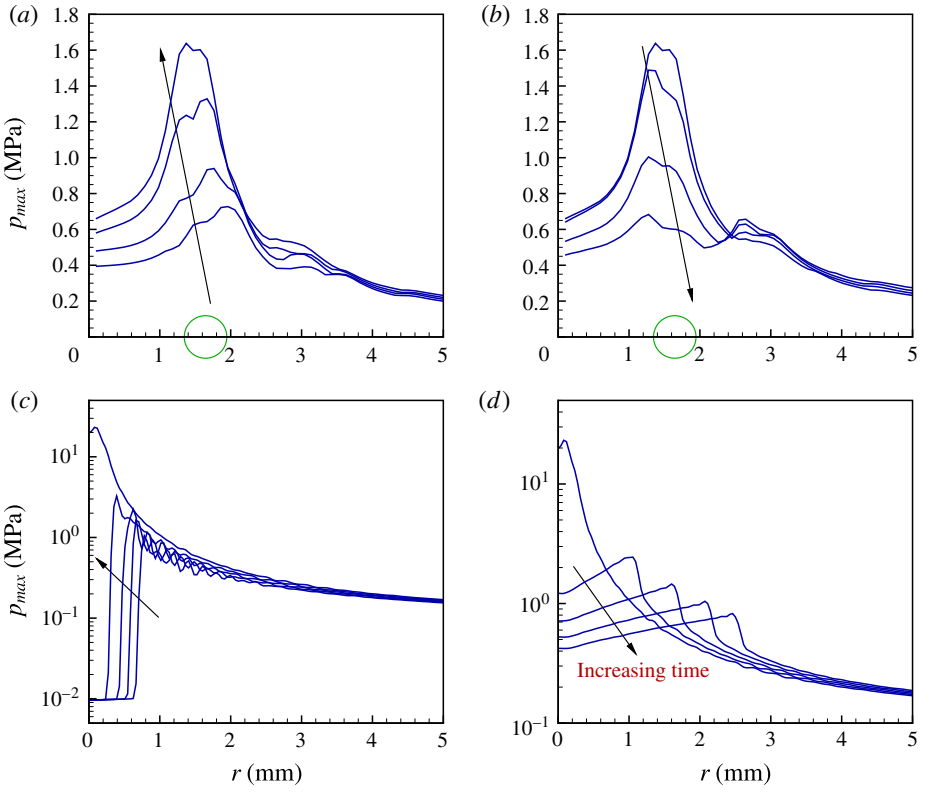


FIGURE 13. (Colour online) (*a*,*b*) Detailed simulations: p_{max} versus r for time ranges (*a*) $t = 391$–397 μs, (*b*) $t = 397$–403 μs, for the special detailed simulation considered in this section. (*c*,*d*) Pressure p along the homogeneous-mixture radius r for times (*c*) $t = 367.5$–371.5 μs, (*d*) $t = 371.5$–375.5 μs.

with radii governed by coupled Rayleigh–Plesset-like equations augmented to account for weak bubble–bubble interactions (Mettin *et al.* 1997; Pelekasis *et al.* 2004). The cluster model we use here for comparison is an extension of the two-bubble Keller–Miksis-like model presented in Mettin *et al.* (1997); it is similar to other cluster models (Doinikov 2004; Bremond *et al.* 2006; Yasui *et al.* 2008):

$$\left(1-\frac{1}{a_1}\frac{\mathrm{D}R_i}{\mathrm{D}t}\right)R_i\frac{\mathrm{D}^2R_i}{\mathrm{D}t^2}+\frac{3}{2}\left(1-\frac{1}{3a_1}\frac{\mathrm{D}R_i}{\mathrm{D}t}\right)\left(\frac{\mathrm{D}R_i}{\mathrm{D}t}\right)^2$$
$$=\frac{1}{\rho_1}\left(1+\frac{1}{a_1}\frac{\mathrm{D}R_i}{\mathrm{D}t}+\frac{R_i}{a_1}\frac{\mathrm{D}}{\mathrm{D}t}\right)(p_{b,i}-p_\infty)-\sum_{j\neq i}\frac{R_j}{d_{ij}}\left[R_j\frac{\mathrm{D}^2R_j}{\mathrm{D}t^2}+2\left(\frac{\mathrm{D}R_j}{\mathrm{D}t}\right)^2\right], \quad (4.6)$$

where R_i and $p_{b,i}$ are the radius and pressure of bubble i, d_{ij} is the separation distance between bubbles i and j, ρ_1 is the liquid density, p_∞ is the pressure in the liquid far away from the bubbles, and a_1 is the speed of sound in the liquid. The summation over all the particle-like bubbles accounts for the leading-order $\sim R_j/r$ component of the pressure field induced by other bubbles; higher-order pressure components, translation of the bubbles, and higher-order liquid compressibility effects are neglected, although they could be included in principle (Doinikov 2004; Ilinskii,

https://doi.org/10.1017/jfm.2015.287 Published online by Cambridge University Press

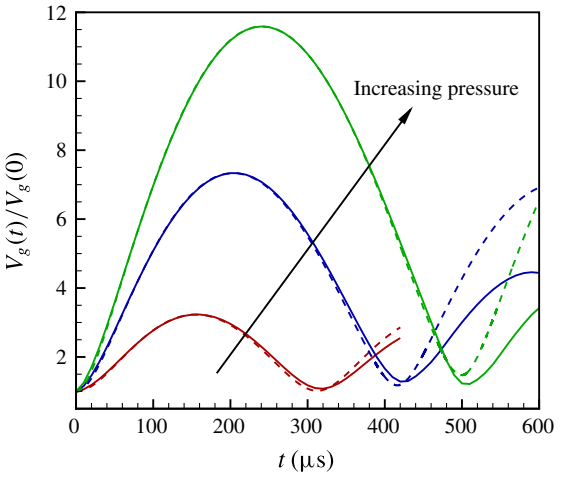


FIGURE 14. (Colour online) Gas volume histories for cases A1 to A3 obtained from: ——, detailed simulations; – – –, the reduced model.

Hamilton & Zabolotskaya 2007; Fuster & Colonius 2011) and some comparisons are available (Fuster *et al.* 2011). Bremond *et al.* (2006) employed a similar model to describe the expansion and collapse of a regular array of 37 bubbles. In that organized configuration, the bubble radii predicted by the model agreed well with their experimental study, except during the collapse phase when the bubbles are obviously non-spherical due to the re-entrant jetting toward the cluster centre. The wall in our configuration acts as a symmetry plane and thus is incorporated in (4.6) via the method of images.

Equation (4.6) is solved for all the cases, with initial radii $R_i(0) = R_0 = 0.3$ mm, and initial velocities $\dot{R}_i(0) = 0$. However, to account for the different initial pressure field assumed in the reduced model compared to the detailed simulation, the initial bubble pressures $p_{b,i}(0)$ are not set to the initial pressure p_g in the detailed simulation; they are set to an adjusted pressure $\tilde{p}_g$, which is obtained such that the maximum gas volume attained in the particle model matches that in the corresponding detailed simulation. We see in figure 14 that the gas volume histories obtained from the reduced model are close to the detailed simulations up to the collapse. Since the bubbles largely remain spherical during the expansion (§ 3), the model is expected to be most successful during this phase. However, as seen in § 3, the bubbles are increasingly aspherical as the collapse propagates inward. Consequently, the reduced model increasingly becomes less accurate and deviates more from the detailed simulations during the cluster collapse, especially after the rebound.

Though the gas volume histories are accurate, peak pressures are significantly different. This is shown in figure 15, where we compare the peak pressures during the final stage of the collapse for the reduced model and detailed simulations. The disagreement increases significantly at higher initial bubble pressures. We see that the particle model overpredicts the peak pressures by nearly a factor of 10 in these most violent cases, when the aspherical dynamics of the bubbles were observed to be most pronounced in § 3. The corresponding pressures on the wall follow essentially the same trend as the bulk pressures. There is a clear trend to this overprediction with increasing pressures, which is consistent with the discussion in § 3.2. Stronger

https://doi.org/10.1017/jfm.2015.287 Published online by Cambridge University Press

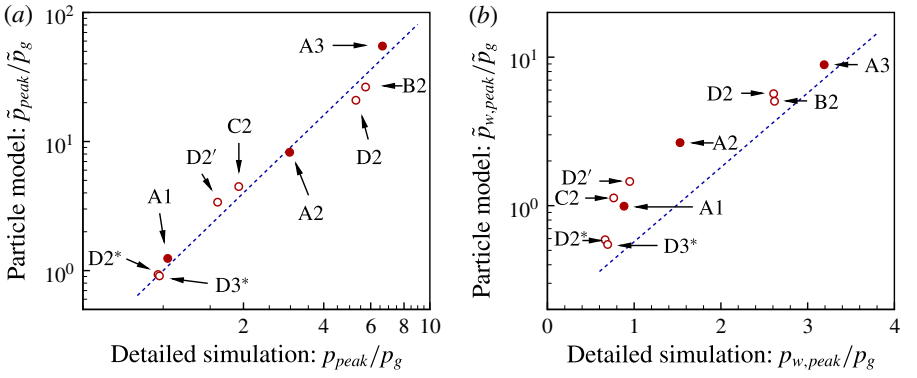


FIGURE 15. (Colour online) Comparison of peak pressure (*a*) in the volume and (*b*) on the wall obtained from detailed simulations and the particle model for cases from table 1 (○), with the common configuration A-series emphasized (●); for reference the dashed line shows $\tilde{p}_{peak}/\tilde{p}_g = p^2_{peak}/p^2_g$ in (*a*) and $\tilde{p}_{w,peak}/\tilde{p}_g = p^2_{w,peak}/p^2_g$ in (*b*).

interactions result in more bubble energy becoming focused into the re-entrant jets and therefore not recoverable for bubble re-expansion. Thus, asymmetric collapses mollify the spherical-bubble peak pressures in a systematic fashion, which suggests a possible correction to predictions based on this reduced model.

5. Summary

The simulations discussed were designed to study the nonlinear dynamics of the bubble clusters including bubble–bubble interactions. Though only a small cluster was considered, the 50 bubbles explicitly represented reproduced the global behaviour visualized in experiments for larger clusters. The initial over-pressure drives an expansion followed by a violent collapse. The gas volume history depends strongly on the initial over-pressure, but is insensitive to the initial arrangement of the bubbles even for this small cluster. The bubbles remain nearly spherical during the expansion phase, but large deformations and topological changes are observed during collapse. The cluster collapse, as suggested by past experimental studies, propagates inward with apparent geometrical focusing, which generates impulsive pressures near the cluster centre. The initial arrangement of the bubbles, particularly the location of the centremost bubble, strongly influences the peak pressures. Some arrangements have over twice the peak pressures near the cluster centre. For a particular arrangement of bubbles, the initial over-pressure is an essential factor in the bubble interactions, with peak pressure increasing by almost a factor of 20 upon changing the initial over-pressure from 0.25 to 0.75 MPa. In general, the bubble shapes show good qualitative agreement with detailed visualizations, such as the regular array studied by Bremond *et al.* (2006).

For comparison, we considered two reduced representations of the cluster dynamics. Despite the lack of a distinct mismatch between the cluster and bubble scale that would justify homogenization, the homogeneous-cloud model provides a reasonable prediction of the overall gas volume history. However, in this case, the regularity of the hemispherical geometry seems to provide a qualitatively different pressure field than the bubble-detailed prediction: the pressure focusing in the homogeneous-mixture model was much more pronounced, suggesting that the nonlinear bubble dynamics

https://doi.org/10.1017/jfm.2015.287 Published online by Cambridge University Press

can, in a sense, mollify the pressure field. Though different in detail, a similar effect is observed for a particle–bubble model. This description reproduces the overall gas volume history even more closely, but significantly overpredicts the peak pressures, which are so elevated because the constituent bubbles are constrained to remain spherical. There was a significantly larger mismatch for cases where there were more pronounced asymmetrical bubble dynamics and jetting. These overpredictions in the particle model seemed to follow a trend, with a regular overprediction for the spherical collapse relative to the corresponding asymmetric collapse. Significantly more statistics would be required to make this conclusive and no detailed explanation for this behaviour has as yet been identified.

Many applications involve significantly larger clusters. However, the small clusters we considered are still important since they show interactions expected to be representative of those in larger clusters. We anticipate that this will be particularly true near the focus of the collapse of a larger cluster, where similar bubble-scale mechanisms can be anticipated to be important. It is possible that the core of a large cluster closely resembles our small cluster, with the collapse focusing on a particular centremost bubble. However, it is also possible that additional length scales could lead to multiple focal-like points in the neighbourhood of the centre of the collapsing cloud. This cannot be directly answered with these simulations; a significantly larger simulation (Rossinelli *et al.* 2013) or more refined diagnostic tools would be needed to investigate this.

Acknowledgement

Portions of this work were supported by NIH grant PO1-DK043881.

Supplementary data

Supplementary data is available at http://dx.doi.org/10.1017/jfm.2015.287.

REFERENCES

D'AGOSTINO, L. & BRENNEN, C. E. 1989 Linearized dynamics of spherical bubble clouds. *J. Fluid Mech.* **199**, 155–176.

AKHATOV, I., LINDAU, O., TOPOLNIKOV, A., METTIN, R., VAKHITOVA, N. & LAUTERBORN, W. 2001 Collapse and rebound of a laser-induced cavitation bubble. *Phys. Fluids* **13** (10), 2805–2819.

ANDO, K., COLONIUS, T. & BRENNEN, C. E. 2011 Numerical simulation of shock propagation in a polydisperse bubbly liquid. *Intl J. Multiphase Flow* **37** (6), 596–608.

ARORA, M., OHL, C. D. & LOHSE, D. 2007 Effect of nuclei concentration on cavitation cluster dynamics. *J. Acoust. Soc. Am.* **121** (6), 3432–3436.

BAER, M. R. & NUNZIATO, J. W. 1986 A two-phase mixture theory for the deflagration-to-detonation transition (DDT) in reactive granular materials. *Intl J. Multiphase Flow* **12** (6), 861–889.

BAILEY, M. R., KHOKHLOVA, V. A., SAPOZHNIKOV, O. A., KARGL, S. G. & CRUM, L. A. 2003 Physical mechanisms of the therapeutic effect of ultrasound - (a review). *Acoust. Phys.* **49** (4), 369–388.

BEST, J. P. 1993 The formation of toroidal bubbles upon the collapse of transient cavities. *J. Fluid Mech.* **251**, 79–107.

BLAKE, J. R. & GIBSON, D. C. 1987 Cavitation bubbles near boundaries. *Annu. Rev. Fluid Mech.* **19**, 99–123.

BLAKE, J. R., KEEN, G. S., TONG, R. P. & WILSON, M. 1999 Acoustic cavitation: the fluid dynamics of non-spherical bubbles. *Phil. Trans. R. Soc. Lond.* A **357** (1751), 251–267.

https://doi.org/10.1017/jfm.2015.287 Published online by Cambridge University Press

BREMOND, N., ARORA, M., OHL, C. D. & LOHSE, D. 2006 Controlled multibubble surface cavitation. *Phys. Rev. Lett.* **96** (22), 224501.

BRENNEN, C. E. 1995 *Cavitation and Bubble Dynamics*. Oxford University Press.

BRENNEN, C. E. 2002 Fission of collapsing cavitation bubbles. *J. Fluid Mech.* **472**, 153–166.

BRUJAN, E. A., IKEDA, T. & MATSUMOTO, Y. 2012 Shock wave emission from a cloud of bubbles. *Soft Matt.* **8** (21), 5777–5783.

BRUJAN, E. A., IKEDA, T., YOSHINAKA, K. & MATSUMOTO, Y. 2011 The final stage of the collapse of a cloud of bubbles close to a rigid boundary. *Ultrason. Sonochem.* **18** (1), 59–64.

BUI, T. T., ONG, E. T., KHOO, B. C., KLASEBOER, E. & HUNG, K. C. 2006 A fast algorithm for modeling multiple bubbles dynamics. *J. Comput. Phys.* **216** (2), 430–453.

CAFLISCH, R. E., MIKSIS, M. J., PAPANICOLAOU, G. C. & TING, L. 1985 Effective equations for wave propagation in bubbly liquids. *J. Fluid Mech.* **153**, 259–273.

CHAHINE, G. L. & DURAISWAMI, R. 1992 Dynamical interactions in a multi-bubble cloud. *Trans. ASME: J. Fluids Engng* **114** (4), 680–686.

COMMANDER, K. W. & PROSPERETTI, A. 1989 Linear pressure waves in bubbly liquids: comparison between theory and experiments. *J. Acoust. Soc. Am.* **85** (2), 732–746.

COUSSIOS, C. C. & ROY, R. A. 2008 Applications of acoustics and cavitation to noninvasive therapy and drug delivery. *Annu. Rev. Fluid Mech.* **40**, 395–420.

DEITERDING, R., RADOVITZKY, R., MAUCH, S. P., NOELS, L., CUMMINGS, J. C. & MEIRON, D. I. 2006 A virtual test facility for the efficient simulation of solid material response under strong shock and detonation wave loading. *Engng Comput.* **22** (3–4), 325–347.

DELALE, C. F. & TUNC, M. 2004 A bubble fission model for collapsing cavitation bubbles. *Phys. Fluids* **16** (11), 4200–4203.

DOINIKOV, A. A. 2004 Mathematical model for collective bubble dynamics in strong ultrasound fields. *J. Acoust. Soc. Am.* **116** (2), 821–827.

ESMAEELI, A. & TRYGGVASON, G. 2004*a* Computations of film boiling. Part I: numerical method. *Intl J. Heat Mass Transfer* **47** (25), 5451–5461.

ESMAEELI, A. & TRYGGVASON, G. 2004*b* Computations of film boiling. Part II: multi-mode film boiling. *Intl J. Heat Mass Transfer* **47** (25), 5463–5476.

FREUND, J. B., COLONIUS, T. & EVAN, A. P. 2007 A cumulative shear mechanism for tissue damage initiation in shock-wave lithotripsy. *Ultrasound Med. Biol.* **33** (9), 1495–1503.

FREUND, J. B., SHUKLA, R. K. & EVAN, A. P. 2009 Shock-induced bubble jetting into a viscous fluid with application to tissue injury in shock-wave lithotripsy. *J. Acoust. Soc. Am.* **126** (5), 2746–2756.

FUSTER, D. & COLONIUS, T. 2011 Modelling bubble clusters in compressible liquids. *J. Fluid Mech.* **688**, 352–389.

FUSTER, D., DOPAZO, C. & HAUKE, G. 2011 Liquid compressibility effects during the collapse of a single cavitating bubble. *J. Acoust. Soc. Am.* **129** (1), 122–131.

GOTTLIEB, S. & SHU, C. W. 1988 Total variation diminishing Runge–Kutta schemes. *Maths Comput.* **67**, 73–85.

HANSSON, I. & MØRCH, K. A. 1980 The dynamics of cavity clusters in ultrasonic (vibratory) cavitation erosion. *J. Appl. Phys.* **51** (9), 4651–4658.

HARDT, S. & WONDRA, F. 2008 Evaporation model for interfacial flows based on a continuum-field representation of the source terms. *J. Comput. Phys.* **227** (11), 5871–5895.

ILINSKII, Y. A., HAMILTON, M. F. & ZABOLOTSKAYA, E. A. 2007 Bubble interaction dynamics in Lagrangian and Hamiltonian mechanics. *J. Acoust. Soc. Am.* **121** (2), 786–795.

JIANG, G. S. & SHU, C. W. 1996 Efficient implementation of weighted ENO schemes. *J. Comput. Phys.* **126** (1), 202–228.

JOHNSEN, E. & COLONIUS, T. 2006 Implementation of WENO schemes in compressible multicomponent flow problems. *J. Comput. Phys.* **219** (2), 715–732.

JOHNSEN, E. & COLONIUS, T. 2009 Numerical simulations of non-spherical bubble collapse. *J. Fluid Mech.* **629**, 231–262.

KAMEDA, M. & MATSUMOTO, Y. 1996 Shock waves in a liquid containing small gas bubbles. *Phys. Fluids* **8** (2), 322–335.

KAMEDA, M., SHIMAURA, N., HIGASHINO, F. & MATSUMOTO, Y. 1998 Shock waves in a uniform bubbly flow. *Phys. Fluids* **10** (10), 2661–2668.

https://doi.org/10.1017/jfm.2015.287 Published online by Cambridge University Press

KELLER, J. B. & MIKSIS, M. 1980 Bubble oscillations of large-amplitude. *J. Acoust. Soc. Am.* **68** (2), 628–633.

KONNO, A., KATO, H., YAMAGUCHI, H. & MAEDA, M. 2002 On the collapsing behavior of cavitation bubble clusters. *JSME Intl J.* B **45** (3), 631–637.

KORNFELD, M. & SUVOROV, L. 1944 On the destructive action of cavitation. *J. Appl. Phys.* **15**, 495–506.

KREFTING, D., METTIN, R. & LAUTERBORN, W. 2004 High-speed observation of acoustic cavitation erosion in multibubble systems. *Ultrason. Sonochem.* **11**, 119–123.

KUBOTA, A., KATO, H. & YAMAGUCHI, H. 1992 A new modelling of cavitating flows: a numerical study of unsteady cavitation on a hydrofoil section. *J. Fluid Mech.* **240**, 59–96.

LAUER, E., HU, X. Y., HICKEL, S. & ADAMS, N. A. 2012 Numerical investigation of collapsing cavity arrays. *Phys. Fluids* **24** (5), 052104.

LAUTERBORN, W. & KURZ, T. 2010 Physics of bubble oscillations. *Rep. Prog. Phys.* **73** (10), 106501.

LINDAU, O. & LAUTERBORN, W. 2003 Cinematographic observation of the collapse and rebound of a laser-produced cavitation bubble near a wall. *J. Fluid Mech.* **479**, 327–348.

MATSUMOTO, Y., ALLEN, J. S., YOSHIZAWA, S., IKEDA, T. & KANEKO, Y. 2005 Medical ultrasound with microbubbles. *Exp. Therm. Fluid Sci.* **29** (3), 255–265.

MATSUMOTO, Y. & YOSHIZAWA, S. 2005 Behaviour of a bubble cluster in an ultrasound field. *Intl J. Numer. Meth. Fluids* **47**, 591–601.

MENIKOFF, R. & PLOHR, B. J. 1989 The Riemann problem for fluid-flow of real materials. *Rev. Mod. Phys.* **61** (1), 75–130.

METTIN, R., AKHATOV, I., PARLITZ, U., OHL, C. D. & LAUTERBORN, W. 1997 Bjerknes forces between small cavitation bubbles in a strong acoustic field. *Phys. Rev.* E **56** (3), 2924–2931.

OMTA, R. 1987 Oscillations of a cloud of bubbles of small and not so small amplitude. *J. Acoust. Soc. Am.* **82** (3), 1018–1033.

PARLITZ, U., METTIN, R., LUTHER, S., AKHATOV, I., VOSS, M. & LAUTERBORN, W. 1999 Spatio-temporal dynamics of acoustic cavitation bubble clouds. *Phil. Trans. R. Soc. Lond.* A **357** (1751), 313–334.

PELEKASIS, N. A., GAKI, A., DOINIKOV, A. & TSAMOPOULOS, J. A. 2004 Secondary Bjerknes forces between two bubbles and the phenomenon of acoustic streamers. *J. Fluid Mech.* **500**, 313–347.

PHILIPP, A. & LAUTERBORN, W. 1998 Cavitation erosion by single laser-produced bubbles. *J. Fluid Mech.* **361**, 75–116.

PISHCHALNIKOV, Y. A., MCATEER, J. A., WILLIAMS, J. C., PISHCHALNIKOVA, I. V. & VONDERHAAR, R. J. 2006 Why stones break better at slow shockwave rates than at fast rates: in vitro study with a research electrohydraulic lithotripter. *J. Endourol.* **20** (8), 537–541.

PLESSET, M. S. & PROSPERETTI, A. 1977 Bubble dynamics and cavitation. *Annu. Rev. Fluid Mech.* **9**, 145–185.

POPINET, S. & ZALESKI, S. 1999 A front-tracking algorithm for accurate representation of surface tension. *Intl J. Numer. Meth. Fluids* **30** (6), 775–793.

POPINET, S. & ZALESKI, S. 2002 Bubble collapse near a solid boundary: a numerical study of the influence of viscosity. *J. Fluid Mech.* **464**, 137–163.

PROSPERETTI, A. & LEZZI, A. 1986 Bubble dynamics in a compressible liquid. Part 1. First-order theory. *J. Fluid Mech.* **168**, 457–478.

RAYLEIGH, LORD 1917 On the pressure developed in a liquid during the collapse of a spherical cavity. *Phil. Mag.* **34**, 94–98.

REISMAN, G. E., WANG, Y. C. & BRENNEN, C. E. 1998 Observations of shock waves in cloud cavitation. *J. Fluid Mech.* **355**, 255–283.

ROBERTS, W. W., HALL, T. L., IVES, K., WOLF, J. S., FOWLKES, J. B. & CAIN, C. A. 2006 Pulsed cavitational ultrasound: A noninvasive technology for controlled tissue ablation (histotripsy) in the rabbit kidney. *J. Urol.* **175** (2), 734–738.

ROSSINELLI, D., HEJAZIALHOSSEINI, B., HADJIDOUKAS, P., BEKAS, C., CURIONI, A., BERTSCH, A., FUTRAL, S., SCHMIDT, S., ADAMS, N. & KOUMOUTSAKOS, P. 2013 11 PFLOP/s simulations of cloud cavitation collapse. In *Proceedings of the International Conference on High Performance Computing, Networking, Storage and Analysis (Supercomputing 2013, SC13)*. Article no. 3. ACM.

https://doi.org/10.1017/jfm.2015.287 Published online by Cambridge University Press

SAPOZHNIKOV, O. A., KHOKHLOVA, V. A., BAILEY, M. R., WILLIAMS, J. C., MCATEER, J. A., CLEVELAND, R. O. & CRUM, C. A. 2002 Effect of overpressure and pulse repetition frequency on cavitation in shock wave lithotripsy. *J. Acoust. Soc. Am.* **112** (3), 1183–1195.

SAUREL, R. & ABGRALL, R. 1999*a* A multiphase Godunov method for compressible multifluid and multiphase flows. *J. Comput. Phys.* **150** (2), 425–467.

SAUREL, R. & ABGRALL, R. 1999*b* A simple method for compressible multifluid flows. *SIAM J. Sci. Comput.* **21** (3), 1115–1145.

SEO, J. H., LELE, S. K. & TRYGGVASON, G. 2010 Investigation and modeling of bubble–bubble interaction effect in homogeneous bubbly flows. *Phys. Fluids* **22** (6), 063302.

SHIMADA, M., MATSUMOTO, Y. & KOBAYASHI, T. 2000 Influence of the nuclei size distribution on the collapsing behavior of the cloud cavitation. *JSME Intl J.* B **43** (3), 380–385.

SMEREKA, P. 2002 A Vlasov equation for pressure wave propagation in bubbly fluids. *J. Fluid Mech.* **454**, 287–325.

TITAREV, V. A. & TORO, E. F. 2004 Finite-volume WENO schemes for three-dimensional conservation laws. *J. Comput. Phys.* **201** (1), 238–260.

TIWARI, A., FREUND, J. B. & PANTANO, C. 2013 A diffuse interface model with immiscibility preservation. *J. Comput. Phys.* **252**, 290–309.

TORO, E. F. 2006 *Riemann Solvers and Numerical Methods for Fluid Dynamics*. Springer.

WANG, Y. C. 1999 Effects of nuclei size distribution on the dynamics of a spherical cloud of cavitation bubbles. *Trans. ASME: J. Fluids Engng* **121** (4), 881–886.

WANG, Y. C. & BRENNEN, C. E. 1999 Numerical computation of shock waves in a spherical cloud of cavitation bubbles. *Trans. ASME: J. Fluids Engng* **121** (4), 872–880.

VAN WIJNGAARDEN, L. 1968 On the equations of motion for mixtures of liquid and gas bubbles. *J. Fluid Mech.* **33** (3), 465–474.

VAN WIJNGAARDEN, L. 1972 One-dimensional flow of liquids containing small gas bubbles. *Annu. Rev. Fluid Mech.* **4**, 369–396.

XU, Z., FOWLKES, J. B. & CAIN, C. A. 2006 A new strategy to enhance cavitational tissue erosion using a high-intensity, initiating sequence. *IEEE Trans. Ultrason. Ferroelectr. Freq. Control* **53** (8), 1412–1424.

XU, Z., FOWLKES, J. B., LUDOMIRSKY, A. & CAIN, C. A. 2005*a* Investigation of intensity thresholds for ultrasound tissue erosion. *Ultrasound Med. Biol.* **31** (12), 1673–1682.

XU, Z., FOWLKES, J. B., ROTHMAN, E. D., LEVIN, A. M. & CAIN, C. A. 2005*b* Controlled ultrasound tissue erosion: the role of dynamic interaction between insonation and microbubble activity. *J. Acoust. Soc. Am.* **117** (1), 424–435.

XU, Z., LUDOMIRSKY, A., EUN, L. Y., HALL, T. L., TRAN, B. C., FOWLKES, J. B. & CAIN, C. A. 2004 Controlled ultrasound tissue erosion. *IEEE Trans. Ultrason. Ferroelectr. Freq. Control* **51** (6), 726–736.

XU, Z., RAGHAVAN, M., HALL, T. L., MYCEK, M.-A., FOWLKES, J. B. & CAIN, C. A. 2008 Evolution of bubble clouds induced by pulsed cavitational ultrasound therapy – histotripsy. *IEEE Trans. Ultrason. Ferroelectr. Freq. Control* **55** (5), 1122–1132.

YASUI, K., IIDA, Y., TUZIUTI, T., KOZUKA, T. & TOWATA, A. 2008 Strongly interacting bubbles under an ultrasonic horn. *Phys. Rev.* E **77** (1), 016609.

ZERAVCIC, Z., LOHSE, D. & VAN SAARLOOS, W. 2011 Collective oscillations in bubble clouds. *J. Fluid Mech.* **680**, 114–149.

ZHANG, D. Z. & PROSPERETTI, A. 1994 Ensemble phase-averaged equations for bubbly flows. *Phys. Fluids* **6** (9), 2956–2970.

ZHANG, S. G., DUNCAN, J. H. & CHAHINE, G. L. 1993 The final stage of the collapse of a cavitation bubble near a rigid wall. *J. Fluid Mech.* **257**, 147–181.

ZHANG, Y. L., YEO, K. S., KHOO, B. C. & WANG, C. 2001 3D jet impact and toroidal bubbles. *J. Comput. Phys.* **166** (2), 336–360.

ZHONG, P., ZHOU, Y. F. & ZHU, S. L. 2001 Dynamics of bubble oscillation in constrained media and mechanisms of vessel rupture in SWL. *Ultrasound Med. Biol.* **27** (1), 119–134.

https://doi.org/10.1017/jfm.2015.287 Published online by Cambridge University Press